Supporting Information

Flexible transparent Ag NWs micromesh electrode with enhanced electrical and thermal properties for multifunctional smart panel application

Zhiwei Fu, [a] He Zhu, [a] Xin Sun, [a] Jikai Yao, [a] Ziyi Dai, [a] Rong Cai,*[b] and Kai Qian*[a,c]

[a.] School of Integrated Circuits, Shandong University, Jinan, 250100, China.

[b.] School of Pharmaceutical Sciences, Shandong University, Jinan, 250012, China.

[c.] Lu'an Branch, Anhui Institute of Innovation for Industrial Technology, Lu'an, 237100, China.

† Rong Cai E-mail: rongcai@sdu.edu.cn. Kai Qian E-mail: kaiqian@sdu.edu.cn

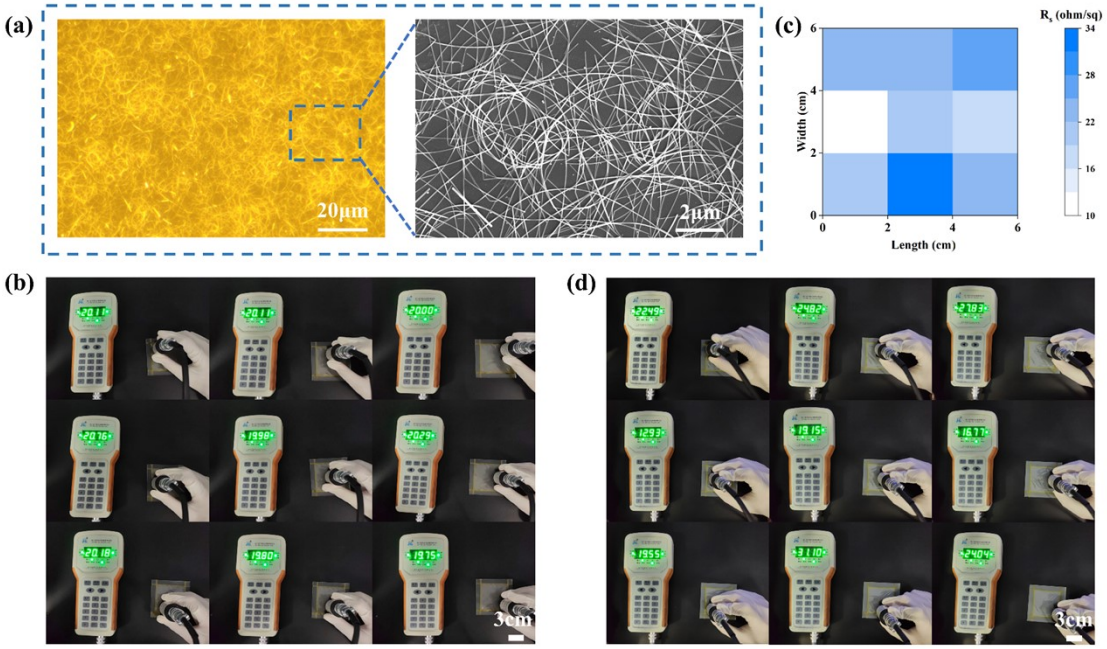

Fig. S1 (a) Optical and SEM images of random Ag NWs networks electrode. (b) Photos of the Ag NMs/eCPI conductor (6 cm × 6 cm) sheet resistance distribution, corresponding to Fig. 1f. (c) Area mapping of the sheet resistance at different positions on the random Ag NWs/eCPI electrode (6 cm × 6 cm), corresponding to the detailed values in the photos (d).

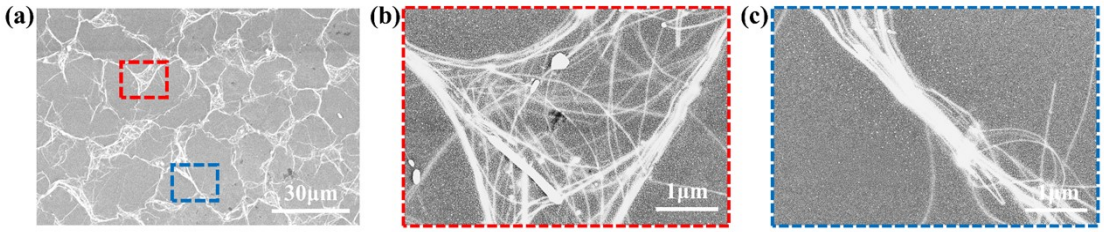

Fig. S2 (a) Surface morphology of Ag NMs/eCPI electrodes (~50 Ω sq^{-1}) after thermal annealing at 300 °C for 3 hours. corresponding to the representative knot (b) and bundle (c) morphology.

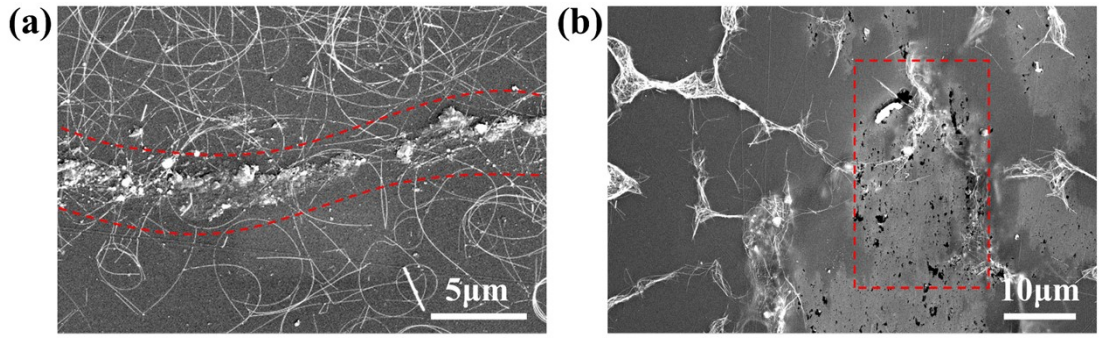

Fig. S3 The wrinkle morphology (a) of r-Ag NWs/eCPI electrode and crack morphology (b) of Ag NMs/eCPI electrode (~50 Ω sq^{-1}, 2 cm × 2 cm) subjected to voltage stress range from 0-20 V (with a voltage ramp of 0.2 V min^{-1}), respectively.

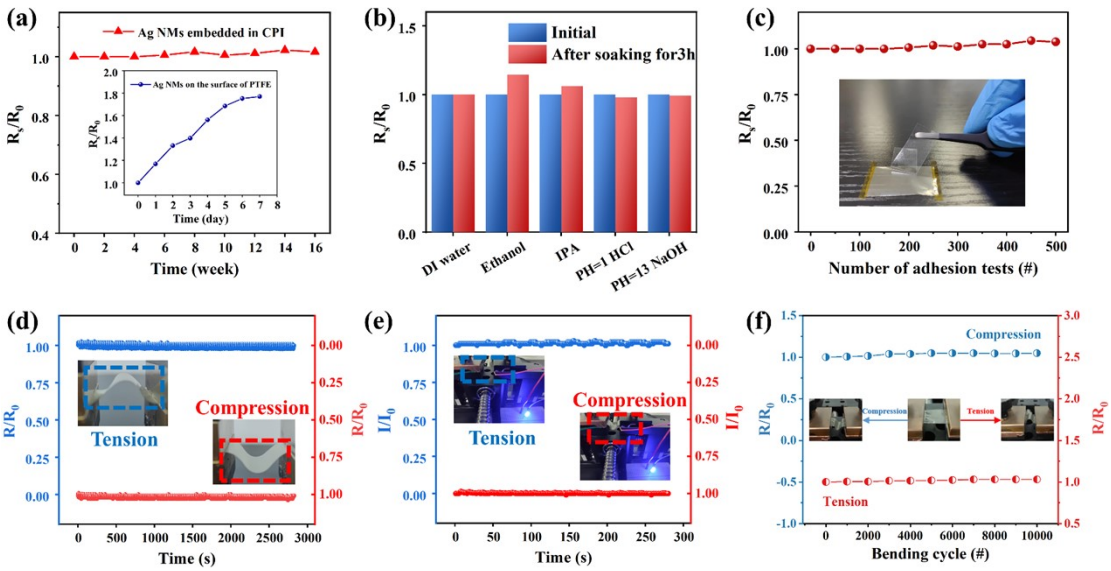

Fig. S4 The Ag NMs/eCPI electrode with superior environmental adaptability and mechanical stability. (a) Sheet resistance change of the Ag NMs/eCPI electrode

exposure to air at room temperature. The inset showed the Ag NMs on PTFE substrate as a comparison to demonstrate the importance of the embedded structure. (b) Sheet resistance change of the Ag NMs/eCPI electrode after immersion in different solvents for 3 hours at room temperature. (c) Sheet resistance change of the Ag NMs/eCPI electrode after the adhesion test with 3M Scotch tape. Real-time monitoring of the resistance (d) and current (e) changes of Ag NMs/eCPI electrode during bending process (r ~1 mm) in tensile and compressive modes. Insets (e) were the photographs of stable LED lighting, which is connected to the Ag NMs/eCPI conductor. (f) Resistance variation of the Ag NMs/eCPI conductors during long-term monitoring of 10000 cycles in tensile and compressive modes (bending radius of ~1 mm). Insets showed the demonstration of electrode bend in tension and compression modes.

Compared to the quick electrical degradation of Ag NMs electrode on substrate surface ($R_s/R_0 > 1.76$) only after 1 week (illustration of Fig. S4a), the Ag NMs/eCPI conductor exhibited quite stable property ($R_s/R_0 < 1.02$) in ambient air even after exposure to air for 16 weeks (Fig. S4a), which also had superior stability in different solvents, such as soaking in deionized water, ethanol, isopropyl alcohol, hydrochloric acid (pH=1) and sodium hydroxide (pH=13) for 3 hours (Fig. S4b). In addition, the results of adhesion and bending tests of Ag NMs/eCPI conductor were depicted in Fig. S4c-f, where the Ag NMs/eCPI electrode showed negligible resistance change. As shown in the Fig. S5, the microstructure of Ag NMs did not show significant change before and after 10000 bending cycles, and the conductive network was still intact, demonstrating the excellent mechanical stability of Ag NMs/eCPI electrode. As a demonstration, Ag NMs/eCPI electrode is connected to a circuit with an LED, and the excellent reliability and flexibility of the electrode is illustrated by the fact that the luminance of the LED remains stable during electrode bending (Fig. S4e and Movie S1). The above results prove that the Ag NMs/eCPI electrode has excellent flexibility and stability in various of harsh environments, demonstrating great potential applications in multi-functional integration electronics.

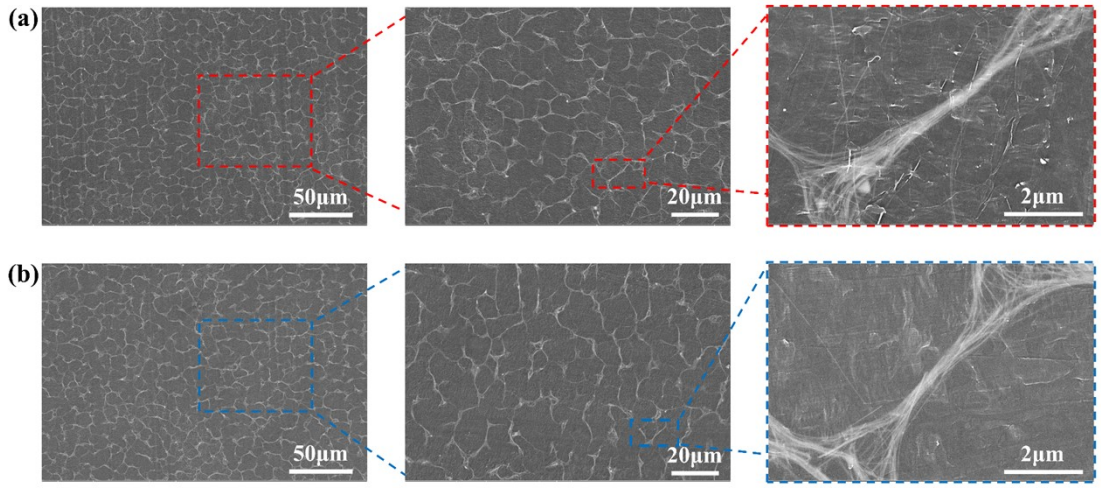

Fig. S5 SEM surface morphology of Ag NMs/eCPI electrode before (a) and after (b)10000 cycles bending.

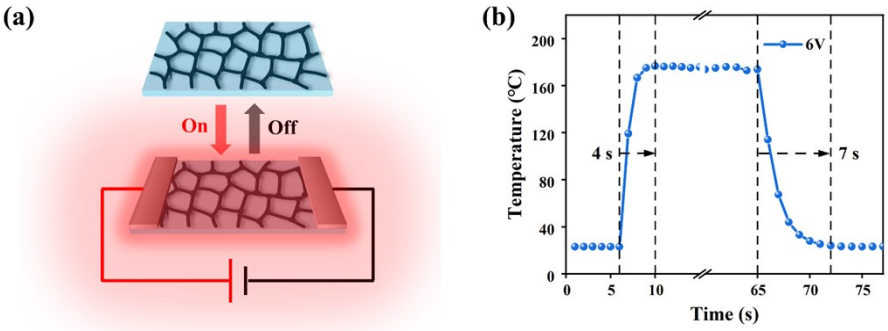

Fig. S6 (a) Schematic diagram of heating and cooling status of Ag NMs/eCPI heater. (b) Heating and cooling times of the Ag NMs/eCPI heater at 6 V constant voltage.

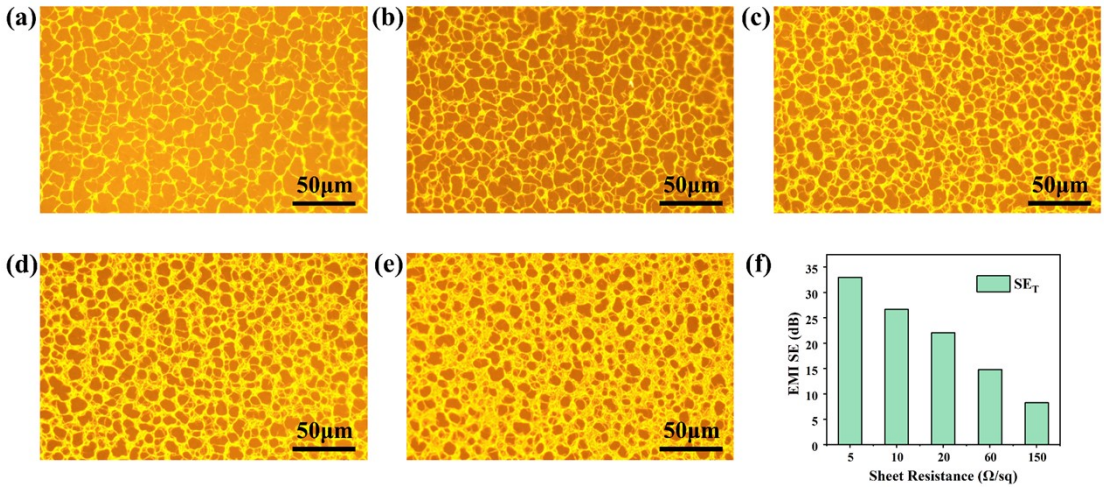

Fig. S7 (a-e) Microscopic morphology images of Ag NMs/eCPI conducting films with

R_s of ~150, ~60, ~20, ~10, and ~5 Ω sq^{-1}, corresponding to their (f) EMI shielding effectiveness (SE_T).

The R_s of Ag NMs/eCPI electrodes could be adjusted by changing the dosage of Ag NWs ink. As shown in Fig. S7a-e, the Ag NMs/eCPI conducting films would exhibit lower sheet resistances (~150, ~60, ~20, ~10, and ~5 Ω sq^{-1}) with more ink and thicker Ag NWs micromeshes. Accordingly, the electromagnetic shielding performance of the Ag NMs/eCPI conducting film will be better with lower sheet resistance (Fig. S7f).

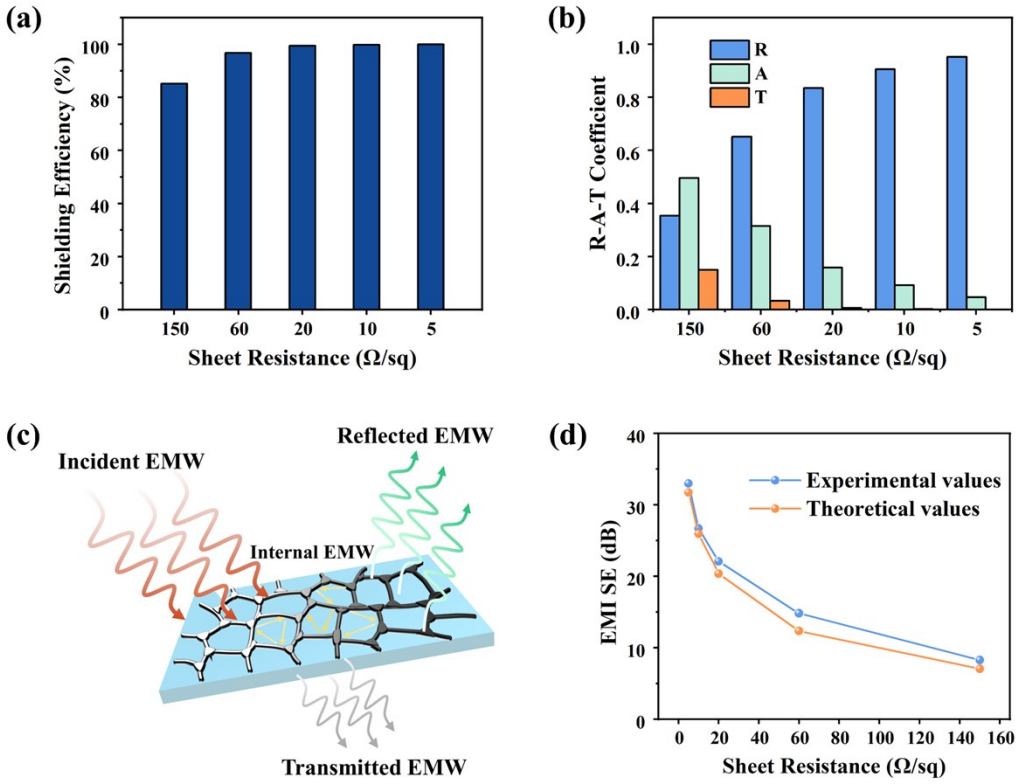

Fig. S8 (a) Shielding efficiency of the flexible transparent Ag NMs/eCPI conducting films with different sheet resistances. (b) Power coefficients A, R, and T of the Ag NMs/eCPI films. (c) Schematic description of EMI shielding mechanism. (d) Comparison between theoretical and experimental values of EMI SE.

To well elucidate the shielding mechanism of Ag NMs/eCPI conductor, the

absorption (A), reflection (R), and transmission (T) coefficients were calculated from measured electromagnetic parameters (calculated by equations 1 in the Experimental Section). At present, many electromagnetic shielding materials such as Mxene, multiwalled carbon nanotubes and graphene nanoplatelets have been developed, and the electromagnetic shielding mechanism also has been elaborated in detail.[1-4] Generally, when electromagnetic radiations encounter EMI shielding materials, part of the waves are reflected on the surface and the remaining portion penetrate into materials, resulting in absorption and multiple reflections. The higher R value in Fig. S8b implyed the primary reflection shielding mechanism, which was consistent with the reported wave-reflection material of Ag due to the impedance mismatch.[5,6] Moreover, the R value increased gradually with sheet resistance decreases of Ag NMs/eCPI conductor, indicating that conductive Ag NWs with abundance of mobile charge carriers reflected most of incident EM waves before absorption and only a very small part can penetrate into the material to be attenuated (Fig. S8c). In addition, there were also multiple internal reflection (Fig. S8c, d) and scattering in the Ag NMs/eCPI conductor due to the multilayers structure of Ag NWs, which transformed the penetrated EMWs into thermal energy.[7,8] To investigate the multiple-reflection effect in Ag NMs/eCPI conductor, the experimental and theoretical EMI SE values of Ag NMs/eCPI conductor were provided (Fig. S8d). If the Ag NMs is monolayer, the theoretical EMI SE values can be calculated based on the following equation:[9,10] EMI SE = $20\lg(1 + Z_0/2R_s)$, where Z_0 (377 Ω) is the wave impedance of free space, R_s is the sheet resistance of Ag NMs. As shown in Fig. S8d, it is obvious that the EMI SE experimental values were always higher than that of Ag NMs conductor with monolayer model, indicating that the interior of Ag NMs/eCPI conductor with multilayers induced multiple reflections and consumed lots of electromagnetic waves.

References

1. Y. Du, Z. Yan, W. You, Q. Men, G. Chen, X. Lv, Y. Wu, K. Luo, B. Zhao, J. Zhang and R. Che, *Adv. Funct. Mater.*, 2023, **33**, 2301449.
2. B. Zhao, Y. Du, H. Lv, Z. Yan, H. Jian, G. Chen, Y. Wu, B. Fan, J. Zhang, L. Wu, D. W. Zhang and R. Che, *Adv. Funct. Mater.*, 2023, **33**, 2302172.
3. B. Zhao, Y. Du, Z. Yan, L. Rao, G. Chen, M. Yuan, L. Yang, J. Zhang and R. Che, *Adv. Funct. Mater.*, 2023, **33**, 2209924.
4. B. Zhao, S. Zeng, X. Li, X. Guo, Z. Bai, B. Fan and R. Zhang, *J. Mater. Chem. C,* 2020, **8**, 500-509.
5. B. Zhou, Q. T. Li, P. H. Xu, Y. Z. Feng, J. M. Ma, C. T. Liu, C. Y. Shen, *Nanoscale*, 2021, **13**, 2378–2388.
6. W. Hong, B. W. Sun, Z. L. Li, Z. W. Fu, J. W. Zhang, M. S. Jiang, Y. Zhang, Y. Li, Y. F. Zhang, K. Qian, *ACS Appl. Electron. Mater*., 2022, **4**, 5446–5455.
7. Y. Shi, Z. Xiang, L. Cai, F. Pan, Y. Dong, X. Zhu, J. Cheng, H. Jiang, W. Lu, *ACS Nano*, 2022, **16**, 7816–7833.
8. B. Zhou, M. Su, D. Yang, G. Han, Y. Feng, B. Wang, J. Ma, J. Ma, C. Liu, C. Shen, *ACS Appl. Mater. Interfaces*, 2020, **12**, 40859–40869.
9. X. Zhu, J. Xu, F. Qin, Z. Yan, A. Guo, C. Kan, *Nanoscale*, 2020, **12**, 14589–14597.
10. J. Gu, S. Hu, H. Ji, H. Feng, W. Zhao, J. Wei, M. Li, *Nanotechnology*, 2020, **31**, 185303.